ELSEVIER

Journal of Fluids and Structures 25 (2009) 1348–1368

JOURNAL OF FLUIDS AND STRUCTURES

www.elsevier.com/locate/jfs

Surface pressure distribution survey in normal triangular tube arrays

J. Mahon*, C. Meskell

School of Engineering, Trinity College Dublin, Ireland

Received 27 June 2008; accepted 22 July 2009
Available online 13 September 2009

Abstract

As a first step towards a validation database for models of fluidelastic instability, an experimental parametric study of the surface pressure on a cylinder in the third row of three normal triangular tube arrays ($P/d = 1.32$, 1.58 and 1.97) with air cross flow has been performed. A range of static tube displacements were examined. Forces were calculated from the pressure measurements providing an understanding of the force generation mechanism. The results show that the fluid forces do not scale proportionally with dynamic head. However, no simple parameterisation was found for the lift force. A bistable flow instability was observed in the pitch ratio of 1.58 even when the tube was displaced. This phenomena resulted in the large asymmetry observed in the pressure distribution around a static cylinder. It is concluded that the fluid forces which are related to fluidelastic instability are dependent on Reynolds number and pitch ratio.

Keywords: Surface pressure distribution; Fluid forces; Fluidelastic instability; Flow instability; Tube arrays

1. Introduction

The mechanism responsible for fluidelastic instability (FEI) in tube arrays has been described by three theoretical frameworks: the "wavy-wall" model (Lever and Weaver, 1986); the quasi-static model (Connors, 1970); and the quasi-steady model (Price and Païdoussis, 1984a). There are also a number of empirical models. In addition, there have been a number of numerical simulations of fluidelastic instability using Large Eddy Simulation, Reynolds Averaged Navier Stokes and vortex methods. These models are based on very different assumptions of the underlying fluid mechanics. A review of the various models can be found in Price (1995). The approach for validating these models depends primarily on the comparison of predicted critical velocity to experimental values. Unfortunately, while this threshold is of greatest interest from a practical point of view, the experimental data available show a significant unexplained scatter. In order to provide an initial validation of the assumptions and predictions of these models, a detailed survey of the surface pressure distribution on a statically displaced cylinder in normal triangular tube arrays has been conducted. While there is already limited pressure data in the literature [e.g., Achenbach (1969), Zdravkovich and Namork (1980), Žukauskas et al. (1983), Ljungkrona et al. (1991)], pressure distributions were measured for only a few Reynolds numbers. Furthermore, there appears to be no comprehensive studies of the pressure field around a statically displaced cylinder

*Corresponding author.
E-mail address: mahonjp@tcd.ie (J. Mahon).

0889-9746/$ - see front matter © 2009 Elsevier Ltd. All rights reserved.
doi:10.1016/j.jfluidstructs.2009.07.006

Nomenclature

C_D	drag coefficient	P	pitch
C_L	lift coefficient	P/d	pitch ratio
C_P	mean pressure coefficient	P_θ	mean pressure at a give position angle
d	tube diameter	$P_{\theta\max}$	mean pressure at stagnation point
F_D	drag force	Re	Reynolds number
FEI	fluidelastic instability	U	free stream flow velocity
F_L	lift force	U_g	gap velocity
l	tube length	y/d	non-dimensionalised tube displacement
NT	normal triangular	$\Delta\theta$	difference between real and actual θ
		θ	position angle
		ρ	fluid density (air)

within a tube array available. Batham (1973) presented a limited study of the pressure distribution around a statically displaced cylinder in an array. The configuration used was a 10 row in-line array with pitch ratio of 1.25. It was reported that the first three rows were displaced by 0.25 mm which corresponds ~0.5% tube displacement and that the pressure distribution "completely changed". However, no detailed results were presented.

There is literature available on the topic of static tube displacements within groups and arrays of cylinders where the fluid force coefficients are measured using a load cell, e.g. Price and Païdoussis (1984b). More recently Ting et al. (1998) used pressure distribution and force measurement techniques to measure the fluidelastic forces on one of two staggered cylinders. Measurements were made for both static and vibrating cylinders for various configurations of two cylinders. However, no pressure distribution data were presented.

2. Experimental set-up

The experimental facility consists of a draw-down wind tunnel which has a tube array installed in the test section. The test-section is 750 mm long with a cross-section of 300 mm × 300 mm. Three tube arrays were investigated in this study. The configurations tested were five row, normal triangular tube arrays with pitch ratios of 1.32, 1.58 and 1.97 with air cross-flow. A schematic of the test-section is shown in Fig. 1.

A pitot-static tube installed upstream of the tube array connected to a Furness Control micromanometer (model FC015) measured the free stream flow velocity in the test section. The flow velocity in the wind tunnel test-section ranged from 2 to 18 m/s with a free stream turbulence intensity of less than 1%. The tubes in the array (38 mm diameter) are rigidly fixed, except for one tube which will be referred to as the instrumented cylinder.

The instrumented cylinder has 36 pressure taps with a diameter of 1 mm and located at the mid-span around the circumference of the cylinder. The centre of the cylinder where the pressure taps are located was constructed from solid brass. Thirty six equispaced holes at 10° intervals were drilled around the circumference. The holes were 1 mm diameter and drilled in the direction of the origin (centre–axial direction) until the 1.59 mm diameter holes drilled in axial

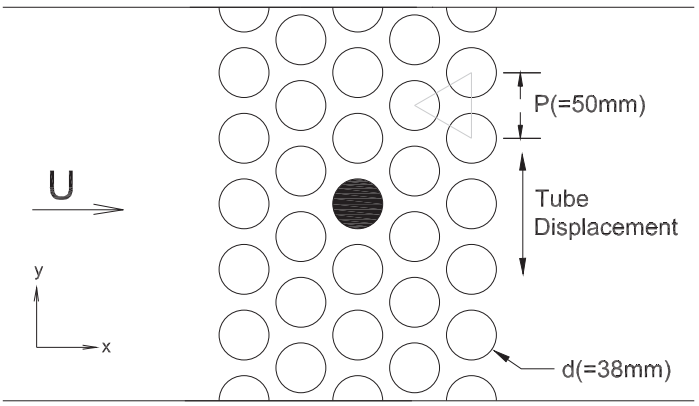

Fig. 1. Test-section schematic; $P/d = 1.32$.

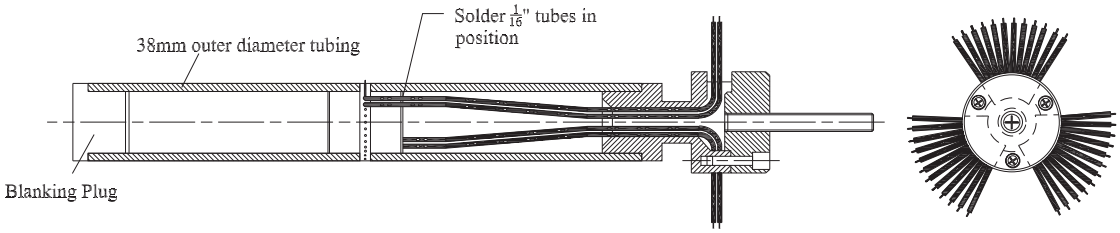

Fig. 2. Schematic of the pressure tap tube.

direction were reached. A 1.59 mm outer diameter brass tubing was fit into the axially drilled holes and air tightness was secured by brazing the connection. Two hollow brass tubes were fitted either side of the machined block. A solid cap and base were push fit. The length of the cylinder assembly within the test section was 299 mm with a diameter of 38 mm. Below that the diameter was reduced to facilitate static displacement of the cylinder with the otherwise rigid array. A schematic of the pressure tap cylinder is shown in Fig. 2.

The instrumented tube was connected to the pressure transducers with short lengths of 2 mm internal diameter silicone tubing. Each pressure tap was monitored with a Senotec differential pressure transducer (24 PC Series). The other port of the pressure transducer was vented to atmosphere. In effect the gauge pressure was measured.

The signal from the pressure transducer was acquired at a sample frequency of 64 Hz and the signal was averaged to give a mean value. No dynamic measurements or high frequency sample rates were used. Hence, only a simple calibration procedure was necessary. A known pressure was applied to a pressure transducer (it will now be referred to as the reference pressure transducer). From this, the sensitivity of the pressure transducer was obtained, i.e. a relationship between the output voltage from the pressure transducer at a known pressure. The other pressure transducers were then calibrated with respect to the reference pressure transducer.

The tube was mounted on a bidirectional traverse (located outside the wind tunnel) allowing a specific static displacement to be applied to the cylinder. The traverse facilitated fine displacements and the displacement was monitored with a clock gauge with an accuracy of up to 0.01 mm.

Local flow velocity measurements were made using a signal hot-wire probe which was rotated to measure both the u and v direction velocity components. The hot-wire anemometer used in this setup was a DISA 55M01 system with a 55M10 Constant-temperature anemometer standard bridge. The readings from the pressure transducers were digitised and logged using an NI 8 channel, 24 bit data acquisition frame. Each channel was simultaneously sampled and automatically low pass filtered to avoid aliasing. Additional information on the test setup including schematics and photographs of the pressure tap tube can be found in Mahon (2008).

3. Results

In the first instance, the experimental set-up was validated by measuring the mean pressure distribution around an isolated cylinder and comparing the results with those in the literature. Measurements were acquired at a sample frequency of 64 Hz and for 120 s. The pressure distribution was nondimensionalised and the results presented in terms of the mean pressure coefficient. The pressure coefficient, C_P, was defined as

$$C_P = 1 - \frac{P_{\theta\max} - P_\theta}{\frac{1}{2}\rho U_g^2}, \tag{1}$$

where $P_{\theta\max}$ refers to the mean pressure at the stagnation point, P_θ refers to the local mean static pressure at a given angular distance (also referred to as position angle) and is defined as the positive clockwise angle starting from the front of the cylinder (see Fig. 3), U_g is the gap velocity ($U_g = U[P/(P-d)]$) and ρ is the fluid density. The pressure coefficient was expressed in this way as taking the free stream static pressure as the reference pressure was not appropriate as the mean static pressure varies throughout the array.

The mean pressure coefficient at a Reynolds numbers of 5.6×10^4 for an isolated cylinder is shown in Fig. 4. The curve compares well with data in the literature (Žukauskas, 1989). However, small differences are observed which are attributed to the lower Reynolds number tested in this study. Surface finish and flow conditions are also reported to be important parameters which could contribute to the slight differences observed. Nonetheless, the comparison with the results from the literature was satisfactory, demonstrating the integrity of the setup.

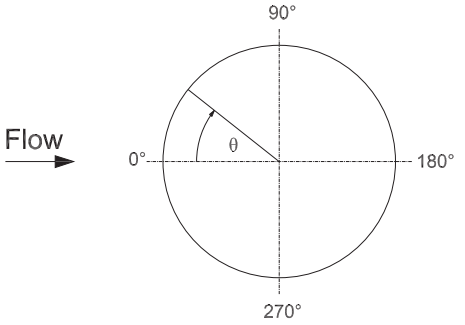

Fig. 3. Schematic of position angle.

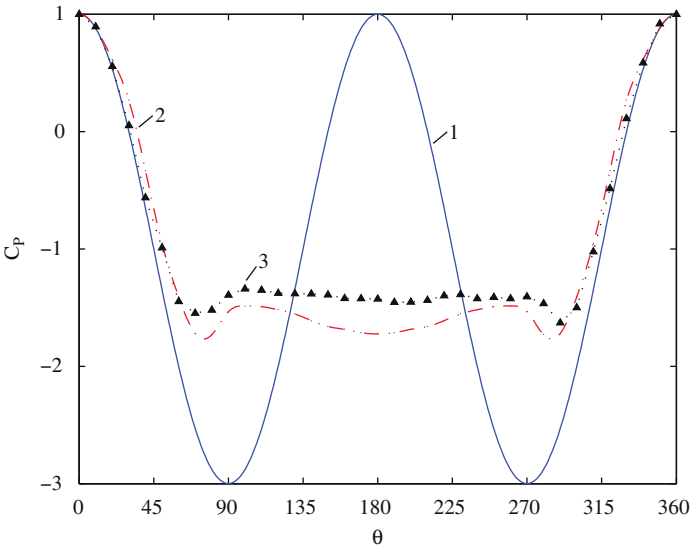

Fig. 4. Distribution of pressure coefficient over the surface of a cylinder: 1 (–), potential flow theory; 2 (– · –), experimental data from the literature ($Re = 8 \times 10^4$), Žukauskas (1989); 3 (▲), experimental data ($Re = 5.6 \times 10^4$), current study.

3.1. Pressure distribution, no displacement

The pressure distributions around a cylinder in the third row of three arrays are presented for a range of Reynolds numbers detailed in Table 1 and static tube displacement in Table 2. Note the Reynolds numbers presented are based on the gap velocities and the tube diameter. C_P for all three arrays at $y/d = 0\%$ is shown in Fig. 5. The neighbouring cylinders in the most compact array of the three have a larger effect as shown by the deceleration of the fluid flowing through the inter-row gap (30°, 330°). The pressure reaches a minimum at the minimum gap (±90°) for $P/d = 1.32$ but this occurs a little earlier (80−90°) for $P/d = 1.58$ and earlier again (70−80°) for $P/d = 1.97$. For all three arrays, the pressure distribution is different to that observed for an isolated cylinder. When the pressure distribution around the whole of the cylinder was examined it revealed that there was a slight asymmetry in the pressure distribution ($P/d = 1.32$). This was attributed to a rotational offset in the position angle. This resulted in a non-zero lift force when the tube was un-displaced ($y/d = 0\%$). However, the offset was quantified and accounted for in the calculation of the lift and drag forces. For $P/d = 1.58$ the pressure distribution was not well behaved showing large asymmetry. In this case the large asymmetry was attributed to flow instability. The pitch ratio of 1.97 also shows asymmetry in the pressure distribution, however, this changed with flow velocity resulting in a peculiar effect with the lift force. This effect will be discussed below.

The effect of Reynolds number was apparent in all three arrays. For $P/d = 1.32$ there was a Reynolds number dependency at lower Reynolds number. As the Reynolds number is increased C_P tended to collapse towards a single

Table 1
Velocities and Reynolds numbers tested.

U (m/s)	$P/d = 1.32$		$P/d = 1.58$		$P/d = 1.97$	
	U_g (m/s)	Re ($\times 10^4$)	U_g	Re ($\times 10^4$)	U_g	Re ($\times 10^4$)
2	8.3	2.23	–	–	–	–
3	12.5	3.34	8.2	2.19	–	–
4	16.7	4.46	10.9	2.92	8.1	2.17
5	20.8	5.58	13.6	3.65	10.1	2.72
6	25.0	6.70	16.4	4.38	12.2	3.26
7	29.2	7.82	19.1	5.12	14.2	3.80
8	33.3	8.93	21.8	5.85	16.2	4.35
9	37.5	10.05	24.5	6.58	18.2	4.89
10	41.7	11.16	27.3	7.31	20.3	5.43
11	–	–	30.0	8.04	22.3	5.98
12	–	–	32.7	8.77	24.3	6.52
13	–	–	35.4	9.50	26.4	7.06
14	–	–	38.2	10.23	28.4	7.60
15	–	–	–	–	30.4	8.15
16	–	–	–	–	32.4	8.69
17	–	–	–	–	34.5	9.23
18	–	–	–	–	36.5	9.78

Table 2
Tube displacement chart.

y/d (%)	0	1	2	3	4	5	6	7	8	9	10	−5
1.32	✔	✔	✔	✔	✔	✔	✔	✔	✔	✔	✔	✔
1.58	✔	✔	✔	✔	✔	✔	–	✔	–	–	✔	✔
1.97	✔	✔	✔	✔	✔	✔	–	✔	–	–	✔	✔

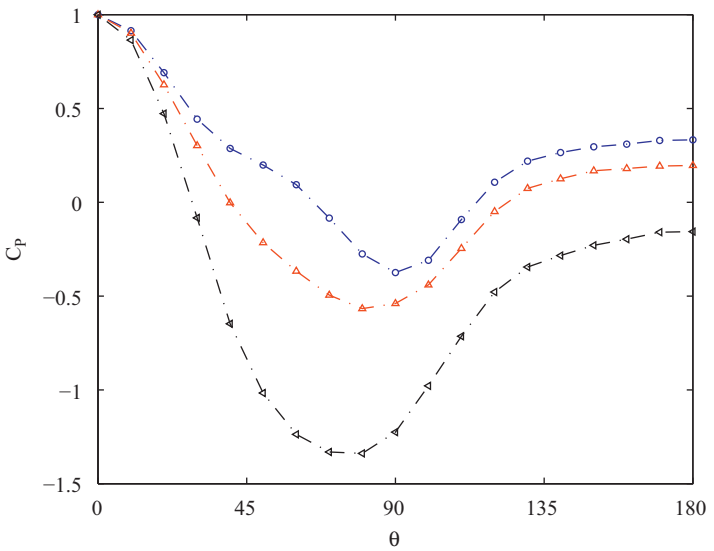

Fig. 5. C_P comparison at the three pitch ratios tested: ○, $P/d = 1.32$, $\mathrm{Re} = 8.93 \times 10^4$; △, $P/d = 1.58$, $\mathrm{Re} = 8.77 \times 10^4$; ◁, $P/d = 1.97$, $\mathrm{Re} = 8.69 \times 10^4$.

constant value at each angular location. When examining C_P at a range of positions around the cylinder (Fig. 6) it was revealed that at the front of the cylinder at higher Reynolds numbers, C_P becomes a constant value, indicating that the pressure in these regions scales proportionally to dynamic head. At the rear and side of the cylinder C_P does not collapse as well, illustrating that the relationship between pressure and dynamic head is not as good. For $P/d = 1.58$ the pressure distribution was found (Fig. 7) to change at all Reynolds numbers tested. It is thought that the reason for the weak relationship between pressure and dynamic head for this array was as a result of the flow instability. For

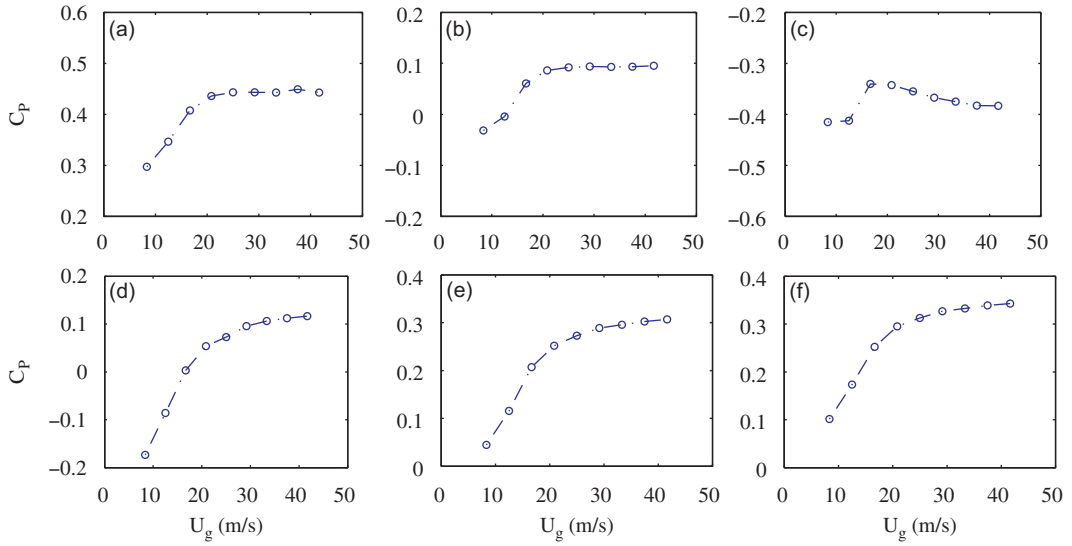

Fig. 6. $P/d = 1.32$; C_P at various positions around the cylinder: (a) $\theta = 30°$; (b) $\theta = 60°$; (c) $\theta = 90°$; (d) $\theta = 120°$; (e) $\theta = 150°$; (f) $\theta = 180°$.

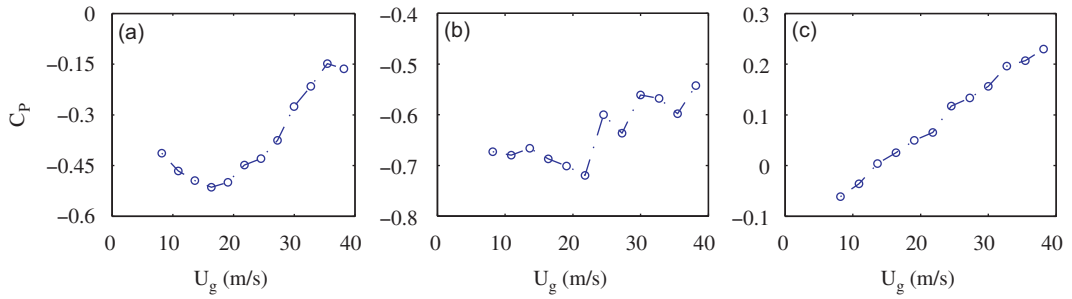

Fig. 7. $P/d = 1.58$; C_P at various positions around the cylinder: (a) $\theta = 60°$; (b) $\theta = 90°$; (c) $\theta = 180°$.

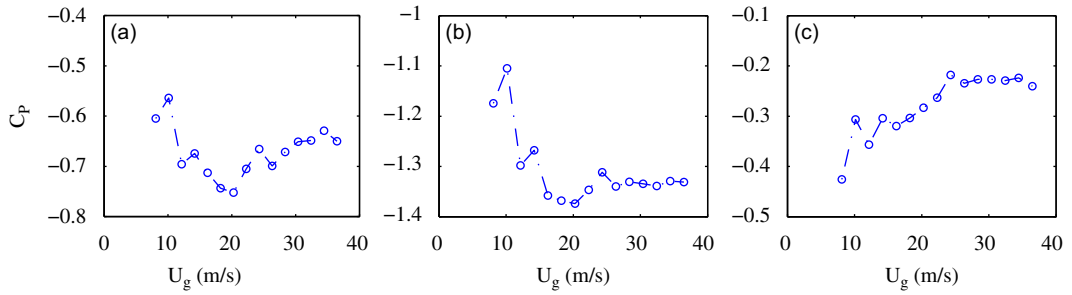

Fig. 8. $P/d = 1.97$; C_P at various positions around the cylinder: (a) $\theta = 60°$; (b) $\theta = 90°$; (c) $\theta = 180°$.

$P/d = 1.97$ there was a Reynolds number dependency at lower Reynolds number. At higher Reynolds numbers C_P collapses well, fluctuating around a constant value (see Fig. 8).

3.2. Pressure distribution, tube displaced

The range of static tube displacement tests conducted are detailed in Table 2. When the tube was displaced, the stagnation point moved in the direction opposite to the tube displacement and this occurred in all three arrays. The change in pressure distribution as a result of tube displacement became less pronounced with increasing pitch ratio. One of the implications of the stagnation point shifting position was that the position of the pressure tap where the total available energy was at its maximum was also shifting. In order to retain the integrity of the nondimensional pressure coefficient and thus facilitate the direct comparison at different tube displacements, the reference pressure was $P_{\theta\max}$, where $\theta_{\max}$ ($= 0^\circ$, undisplaced cylinder) is the position of the maximum pressure which varied depending on tube displacement and the pitch ratio used. In the pitch ratio of 1.58 the adverse effects from the flow instability were also observed at the reference pressure position. Therefore, using the pressure coefficient would not have yielded reliable results. In this section the pressure distribution rather than the pressure coefficient is used to present the results for the pitch ratio of 1.58.

Before examining the effect of tube displacement for the range of displacements outlined in Table 2, tests were conducted to determine if positive and negative displacement was important. Fig. 9 presents data for both positive and negative tube displacement of 5%. Results are shown for two Reynolds numbers. The data obtained from $y/d = -5\%$ was transposed and plotted with the data obtained from $y/d = +5\%$. For both Reynolds numbers the data collapses reasonably well especially at the front and rear of the cylinder. At the top and bottom of the cylinder the scatter was increased slightly which was as a result of the asymmetry due to the slight rotational offset in the position angle. Nonetheless, the data collapse well and it is therefore acceptable to examine the displacement of the cylinder in the positively defined direction only.

Figs. 10, 11 and 12 plot the surface pressure distribution around a cylinder in the third row for a number of static tube displacements for the pitch ratios of 1.32, 1.58 and 1.97, respectively. Some general trends emerged that apply to all pitch ratios. The stagnation point moved in the direction opposite to the tube displacement. For the pitch ratio of 1.32, the rate at which the stagnation point moves with tube displacement was related to Reynolds number. The shift in stagnation point increased with decreasing Reynolds number. As the array pitch increases the shift in the stagnation point reduces. For $P/d = 1.58$ the presence of the flow instability makes it difficult to categorically report a Reynolds number effect with respect to the shift in the stagnation point. As the pitch ratio ($P/d = 1.97$) increases the shift in the stagnation point reduces further.

As detailed previously the most significant changes as a result of tube displacement occurred in the more compact arrays which is not surprising as the geometry was the most restrictive. The largest change in the pressure coefficient occurred where the gap between cylinders was smallest (90°, 270° and inter-row 30°, 330°). This was as a result of the change in the flow velocity in those regions which was caused by the change in the blockage. For $P/d = 1.58$ the largest changes occurred at the minimum gap and to a lesser extent at the inter-row gap. Furthermore, the occurrence of jet switching sometimes obscured the effect of the tube displacement as well as affecting the reference pressure used in C_P. Consequently, using pressure coefficient data to examine the effect of tube displacement in the pitch ratio of 1.58 would have yielded unreliable results. Hence, the results presented for $P/d = 1.58$ are presented in terms of pressure.

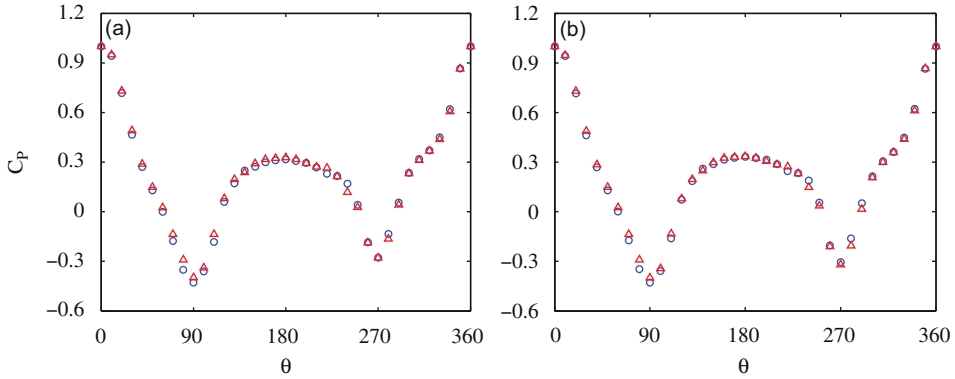

Fig. 9. $P/d = 1.32$; comparison of C_P for: △, $y/d = +5\%$; ○, $y/d = -5\%$. (a) $\mathrm{Re} = 6.7 \times 10^4$; (b) $\mathrm{Re} = 1 \times 10^5$.

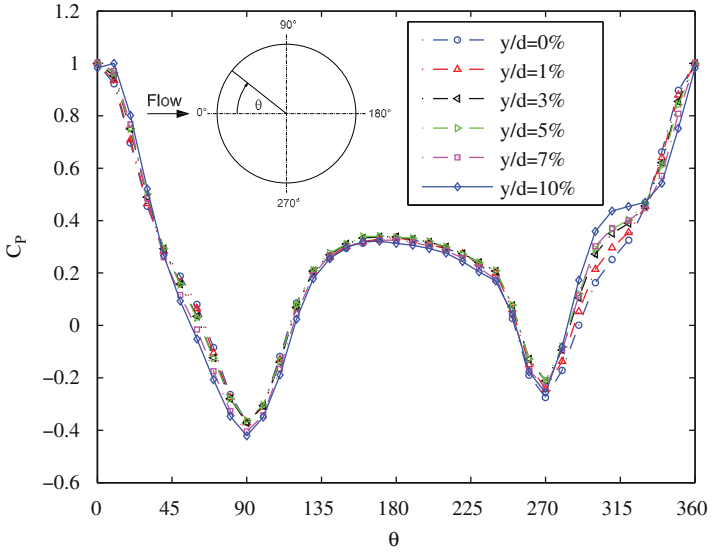

Fig. 10. $P/d = 1.32$; C_P at various tube displacements, $U = 7\,\mathrm{m/s}$ ($\mathrm{Re} = 7.82 \times 10^4$).

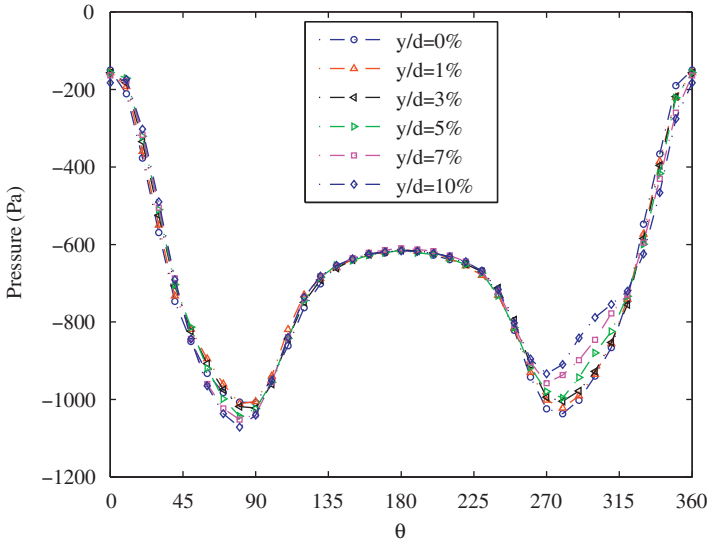

Fig. 11. $P/d = 1.58$; pressure distribution at various tube displacements, $U = 11\,\mathrm{m/s}$.

As the pitch ratio was increased ($P/d = 1.97$) the effect of tube displacement was negligible. In fact, the largest change as a result of tube displacement occurred at the front of the cylinder and not at the minimum gap between neighbouring cylinders. This suggests that the effect of the neighbouring cylinders was small in this instance.

For all array pitches, on the side of the cylinder where tube displacement resulted in increased blockage (330−360°), there was a drop in pressure with tube displacement. The contrary was true on the far side of the cylinder. For $P/d = 1.32$ the inter-row gap (30°, 330°) is a pivot point with the pressure drop switching to a pressure recovery and *vice versa* on the opposite side of the cylinder. For $P/d = 1.58$ the inter-row gap only becomes apparent on the side of the cylinder where the gap between neighbouring cylinders was reduced (blockage increased) when the tube was displaced. In this case the transformation region was larger and the switch was more gradual. For tube displacements up to 5% there was a larger transformation period from approximately 320° to 290°. At the larger tube displacements $>5\%$, the switch in the trend occurs as far forward as $\theta = 320°$ and the pressure recovery was larger. On the opposite side of the cylinder (minimum gap increases) a slight increase in pressure occurs as far back as 60−70° from the front of

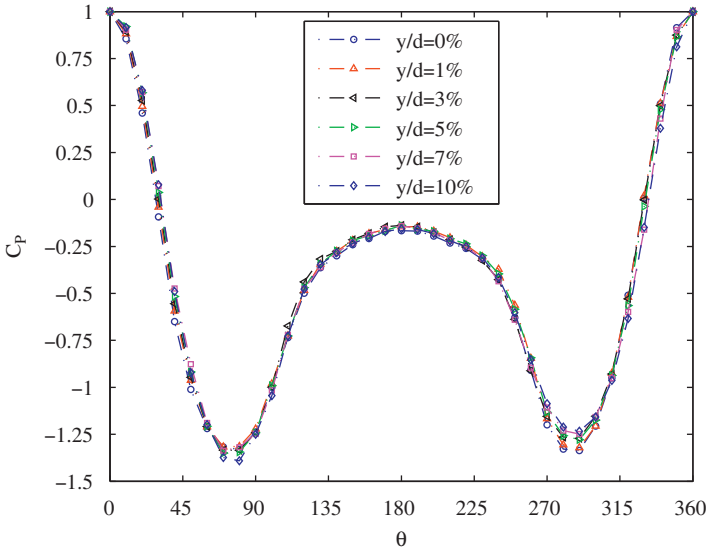

Fig. 12. $P/d = 1.97$; C_P at various tube displacements, $U = 18\,\mathrm{m/s}$ ($\mathrm{Re} = 9.78 \times 10^4$).

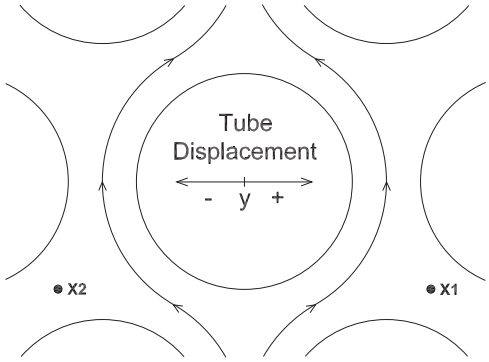

Fig. 13. Schematic of tube geometry for $P/d = 1.32$ showing the location of local flow velocity measurements.

the cylinder. Beyond the transformation region, a pressure drop becomes a pressure recovery. For $P/d = 1.97$ the change in the pressure distribution as a result of tube displacement is less distinct. Nonetheless, the trend of reducing pressure with tube displacement on the side of the cylinder with increased blockage (with tube displacement) reverses at the region of minimum pressure ($280-290^\circ$). The reverse trend occurs on the opposite side of the cylinder.

In an attempt to further understand the pressure data, local flow velocity measurements were made with a single hot-wire probe (see Fig. 13 for locations). Measurements at $\theta = 270^\circ$ in $P/d = 1.32$ showed that when the blockage increases with tube displacement, the pressure increases whilst the flow velocity in this region decreases. This is different to what might be expected; that is, as the gap between neighbouring cylinders reduces, the velocity would increase but this does not occur. This would imply that the flow redistribution occurs after the inter-row gap. In fact at position x_1 in Fig. 13, the magnitude of velocity measured reduces as the tube was displaced supporting the argument of flow redistribution. This was observed at all the Reynolds numbers that were tested. On the opposite side of the cylinder the drop in pressure would be accompanied by an increase in velocity in a potential flow but this was not the case implying that non-recoverable pressure losses are occurring in this region. One possible explanation for the non-recoverable pressure losses was the fact that at position x_2, the magnitude of flow velocity increases with reducing blockage on that side of the cylinder. Hence, the mixing effect of the merging streamtubes was greater resulting in additional losses of the non-recoverable type.

As the position angle moves towards $\theta = 110^\circ$ the trend showing a drop in pressure continues. On the opposite side of the cylinder the pressure recovery continues. At the rear of the cylinder, the pressure increases slightly but the rate at

which the pressure increases varies at each pressure tap, resulting in the non-symmetric pressure distribution shown in this region. This is not surprising as there are considerable differences between the distribution at the front and sides of the cylinder as a result of tube displacement; and if the distribution remained symmetric at the rear it would suggest that the differences observed at the front of the cylinder were not significant, which is known not to be the case. Furthermore, the asymmetry at the rear of the cylinder lends weight to the argument that the mass flow rate does not split equally either side of the cylinder when the tube was displaced. Hence, at the rear of the cylinder the flow velocity changes on either side accordingly thus resulting in a smooth transition as the flow merges at the back of the cylinder. This argument is supported by the fact that there was no increase in C'_P at the rear of the cylinder when the tube was displaced.

For $P/d = 1.58$, at the minimum pressure ($80-90^\circ$) a variation in the pressure exists but it appears to fluctuate around a mean value for displacements up to 5%. As the displacement was increased to 7% and 10%, there was a pressure drop at all Reynolds numbers. At the highest Reynolds number tested ($U = 14\,\mathrm{m/s}$) the effect of the flow instability was less significant. Furthermore, the variation in pressure was considerably smaller, suggesting that the larger variation at the other Reynolds numbers was augmented by the flow instability. Irrespective of Reynolds number, the mean pressure at $\theta = 270-280^\circ$ was found to increase with tube displacement with the largest change in pressure observed in this region; although at times the trend was broken as a result of the flow instability.

On the side of the cylinder where the blockage was reduced, there was a pressure drop at the rear of the cylinder. The opposite trend emerges on the far side of the cylinder. This was quite pronounced at some Reynolds numbers. It is likely that this results from the flow instability. Generally changes would occur, but not to such an exaggerated degree. Further back at the rear of the cylinder, at the lower Reynolds numbers there was an increase in the pressure with increasing displacement similar to that observed for the pitch ratio of 1.32. As the Reynolds number was increased, the rate of increase in pressure recovery reduces. At the higher Reynolds numbers ($>6.6 \times 10^4$) the pressure distribution becomes self-similar. At a comparable Reynolds number a change in the drag force behaviour was also observed suggesting a change in the flow regime. This will be discussed later. For $P/d = 1.97$ there were no significant changes in pressure at the rear of the cylinder. This was not surprising as there were only minimal changes on the front face of the cylinder. Hence, no significant reorganisation of the flow occurred.

3.3. Flow instability

As highlighted above, the mean pressure distribution for the pitch ratio of 1.58 showed significant asymmetry. When tests were repeated the pressure distribution changed (most noticeably in the region of the minimum gap between neighbouring cylinders) suggesting that the asymmetry distribution was due to flow instability. Similar observations have been reported previously in the literature [for example Zdravkovich and Stonebanks (1990), Zdravkovich (1993) and others]. Further investigation demonstrates that flow instability was the cause. Examination of the time resolved pressure signals (Fig. 14), shows that there is significant variation in the pressure. At some positions where the asymmetry was more pronounced, there appeared to be a bi-stable flow regime (jet switching). Additional tests examining the local velocity field are also in agreement as demonstrated by the local flow velocity measurement at $\theta = 20^\circ$ (Fig. 15(a)). Fig. 15(b) shows a histogram of the measurement where it is dominated by a bimodal distribution characteristic of jet switching.

Most interestingly, the flow instability (jet switching) also occurred even when geometric symmetry was broken (i.e. for non-zero tube displacement) and at all displacements ($y/d = 1-10\%$) tested. An example of the bistable flow instability when the tube is displaced ($y/d = 5\%$) is shown in Figs. 16 and 17.

It appears that the nature of the flow instability changes somewhat at the larger displacements. Examining the pressure distribution with the standard deviation imposed (Fig. 18) shows that the deviation was increased on the front face of the cylinder. Examination of the temporal pressure signal reveals bistable flow (jet switching) occurs in this region. The nature of the fluid in a Coanda effect is for the fluid to follow the curvature of the body. Hence, it is not unreasonable to suggest that this was the case—the fluid followed the curvature of the leeward cylinders and detached at some point. When the displacement was small; the detached fluid impinges in the region $40-70^\circ$ and $290-320^\circ$, and as the displacement is increased this moves towards $\theta = 350^\circ$. Flow visualisation was attempted to further understand the nature of the flow but this was inconclusive.

3.4. Fluid forces

Fluid forces associated with fluidelastic instability are dependent on structural motion. Hence, fluid forces associated with fluidelastic instability on a static cylinder do not exist. However, it is possible to estimate the fluidelastic forces

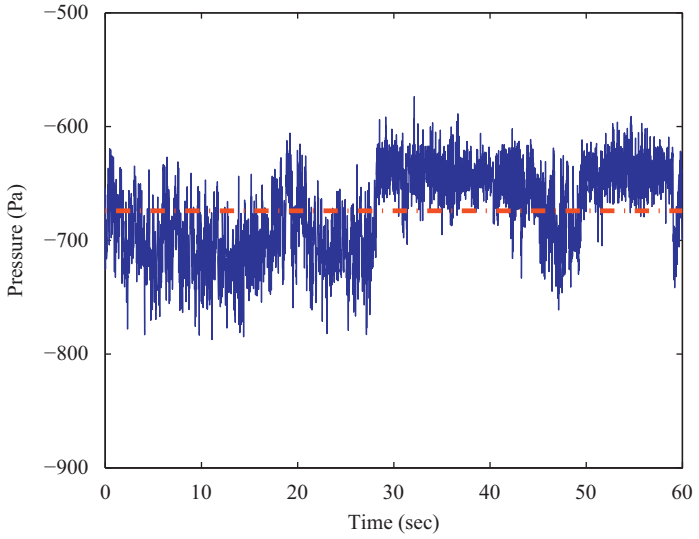

Fig. 14. Time resolved pressure signal; $y/d = 0\%$ at $\theta = 230^\circ$.

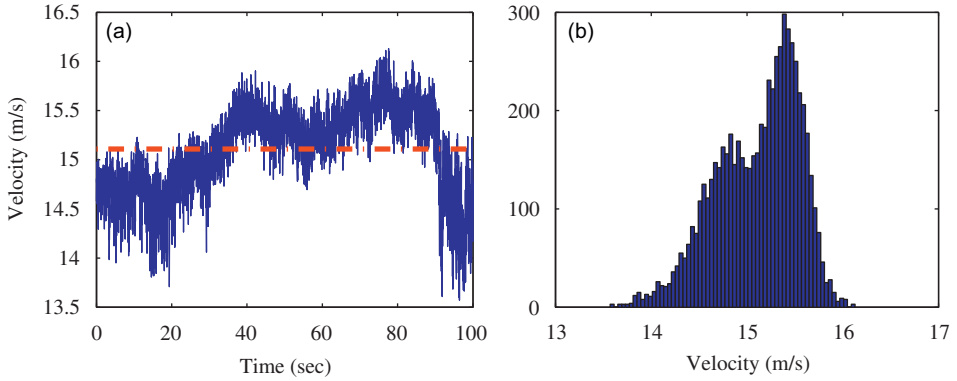

Fig. 15. Local velocity signal (v-direction), $y/d = 0\%$ and $\theta = 20^\circ$; (a) time trace; (b) histogram of time trace.

from static measurements made on a displaced body, but it must be clear that this is not the same thing. This approach has been employed by many researchers in modelling fluidelastic instability (quasi-steady analysis). For example, Price and Païdoussis (1984a) separated the fluidelastic force into a magnitude dependent on the static fluid force and a phase dependent on the time delay. Eq. (2) shows the formulation for the fluidelastic force in the y direction (lift force direction) used by Price and Paidoussis:

$$F_y = \frac{1}{2} U^2 l d \left[e^{-i\omega\Delta t} \left(\frac{\partial C_L}{\partial y} \right) y - C_{D_0} \left(\frac{\dot{y}}{U} \right) \right], \tag{2}$$

where $\partial C_L/\partial y$ is the change in lift coefficient with tube displacement and C_{D_0} is the drag coefficient at zero displacement. It is also clear from Eq. (2) that Price and Paidoussis assume that the fluid forces scale proportionally to dynamic head. This assumption has also been made by other researchers.

In the current study, the fluid forces were obtained by decomposing the surface pressure distribution around the cylinder into the in-flow drag force and the normal lift force components. The asymmetry due to the rotational offset in the position angle as discussed above was quantified and accounted for when calculating the lift and drag forces. The equation for calculating the drag force which takes account of the rotational offset in tube position angle is

$$F_D = -\int_0^{2\pi} P\, dl \cos(\theta + \Delta\theta)\, d\theta, \tag{3}$$

where $\Delta\theta$ is the difference in position angle (difference between the actual 0° and the measured assumed 0°). Similarly, the lift force was modified in the same manner.

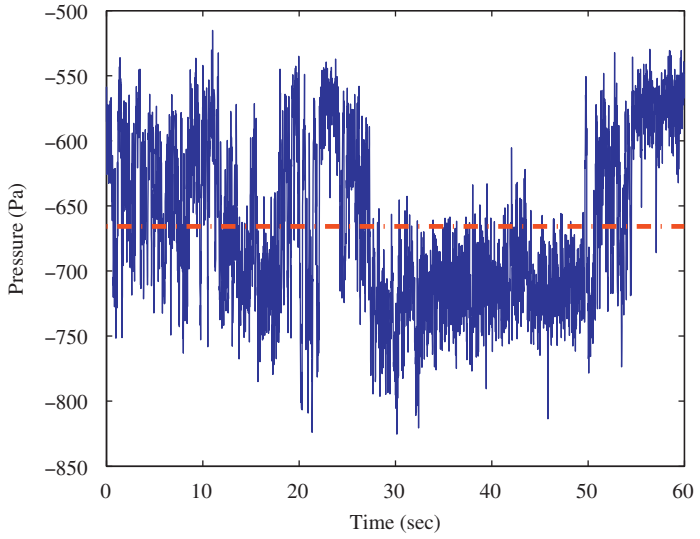

Fig. 16. Time resolved pressure signal; $y/d = 5\%$ at $\theta = 250^\circ$.

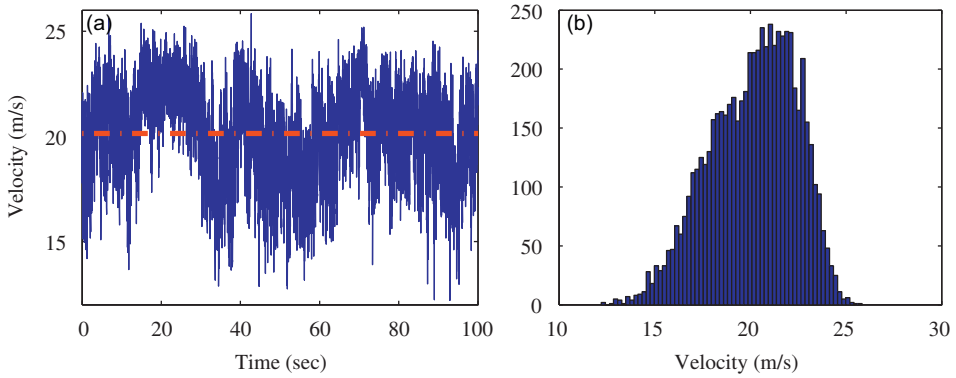

Fig. 17. Local velocity signal (v-direction), $y/d = 5\%$ and $\theta = 70^\circ$; (a) time trace; (b) histogram of time trace.

3.4.1. Drag force

The drag force on a cylinder is composed of skin friction and pressure drag forces. In the current study, the lowest Reynolds number tested was greater than 2×10^4. At these Reynolds numbers, skin friction forces are small and can be neglected. The drag force data is also presented in terms of the nondimensioned drag coefficient,

$$C_D = \frac{F_D}{\frac{1}{2}\rho d l U_g^2}. \tag{4}$$

Fig. 19 plots the drag force against the gap velocity for the pitch ratio of 1.32. Note both scales are logarithmic. The data collapses well using a single line indicating that the drag force is proportional to a power of the gap velocity (see Eq. (5)). The resultant index, n_1, obtained was 1.67. Note the drag force did not scale proportionally to dynamic head as assumed by models in the literature e.g. Price and Païdoussis (1984a).

$$F_D = k_1 U_g^{n_1}. \tag{5}$$

Inserting Eq. (5) into Eq. (4) gives the gap velocity in terms of nondimensional drag coefficient:

$$C_D = k_2 U_g^{n_1 - 2}. \tag{6}$$

Replacing the gap velocity terms with Reynolds number yields

$$C_D = k_3 \mathrm{Re}^{n_2}, \tag{7}$$

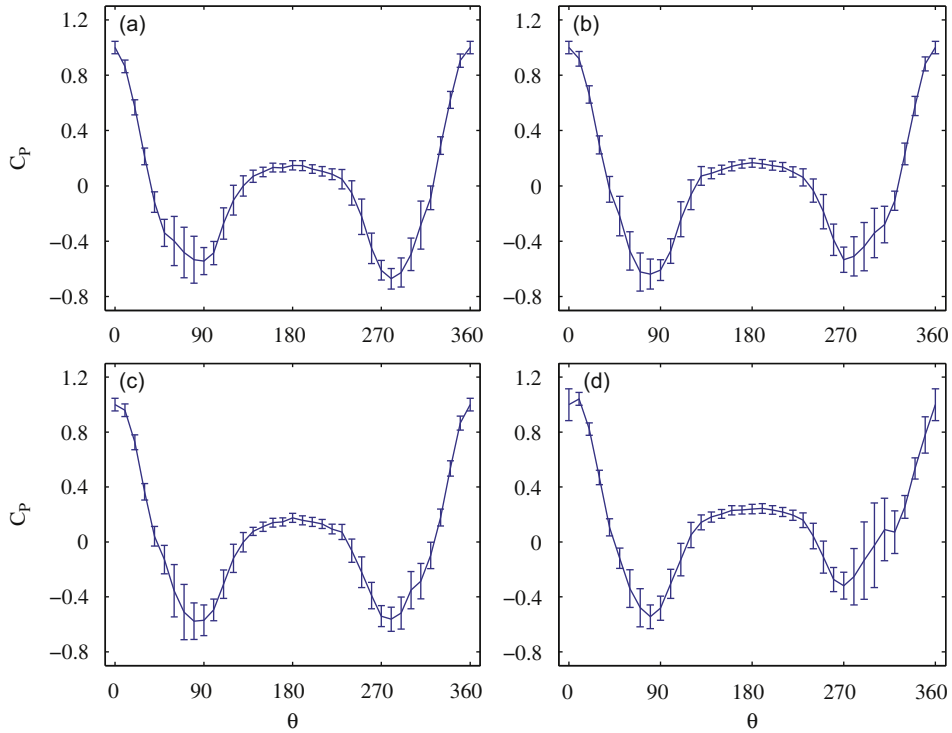

Fig. 18. Pressure coefficient at $U = 11\,\mathrm{m/s}$ and various tube displacements illustrating the deviation from the mean as a result of the flow instability: (a) $y/d = 0\%$; (b) $y/d = 3\%$; (c) $y/d = 5\%$; (d) $y/d = 10\%$.

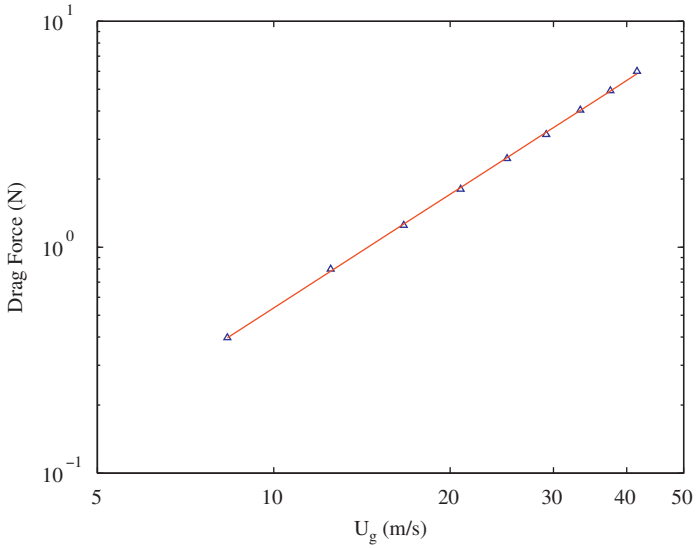

Fig. 19. $P/d = 1.32$; drag force, $y/d = 0\%$.

where $n_2 = n_1 - 2$ and Eq. (7) is a fully nondimensional form illustrating the relationship between drag coefficient and Reynolds number.

When the tube was displaced the system behaved similarly with a line fitting the data sets as shown in Fig. 20.

Fig. 21 plots the extracted indices (in the form of n_2) against tube displacement. The index generally increases with tube displacement. A linear fit was applied to this data ($n_{(y/d)} = 0.00859 \times (y/d) - 0.314$). Using this result the

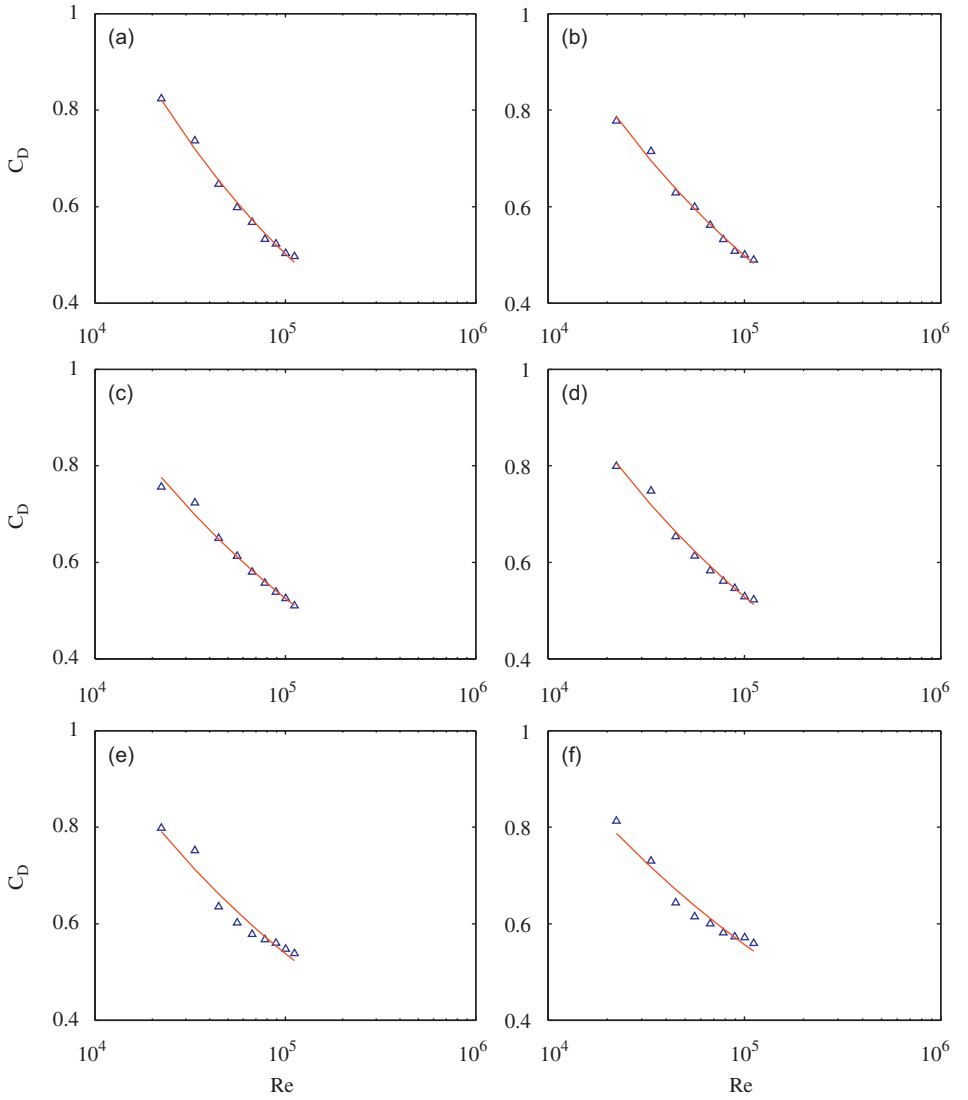

Fig. 20. $P/d = 1.32$; drag coefficient against Reynolds number at various tube displacements: (a) $y/d = 0\%$; (b) $y/d = 1\%$; (c) $y/d = 3\%$; (d) $y/d = 5\%$ (e) $y/d = 7\%$; (f) $y/d = 10\%$.

relationship between drag coefficient and Reynolds number for all static tube displacements is formed:

$$C_D = k_{(y/d)}\mathrm{Re}^{n_{(y/d)}}. \tag{8}$$

The constant $k_{(y/d)}$ was obtained by fitting a quadratic curve to the data,

$$k_{(y/d)} = 0.0479 \times (y/d)^2 - 1.56 \times (y/d) + 18.5. \tag{9}$$

For $P/d = 1.58$ the scatter in the drag force increased as demonstrated in Fig. 22. This was attributed to the flow instability observed in this array. Increasing the duration of the tests and averaging the repeated tests reduced the spread in the data. It was also observed that the effect of tube displacement was smaller than that observed in the denser array and that the most significant changes arising in the pressure distribution from the tube displacement occurred at the top and bottom of the cylinder where the contribution to the drag force was small. Having observed that the effect of tube displacement on the drag force was small, the drag force at all tube displacements was then collapsed onto a single plot and averaged (Fig. 23). Again, logarithmic scaling was used. The data collapses well using two lines. Indices

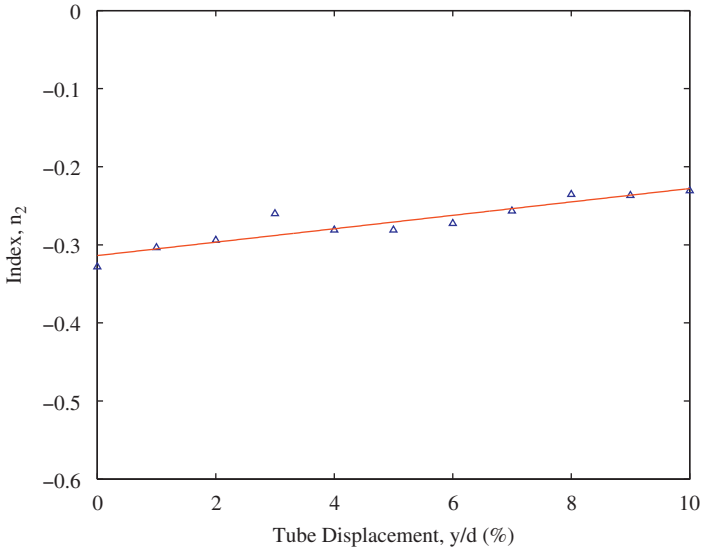

Fig. 21. $P/d = 1.32$; index relating drag coefficient and Reynolds number.

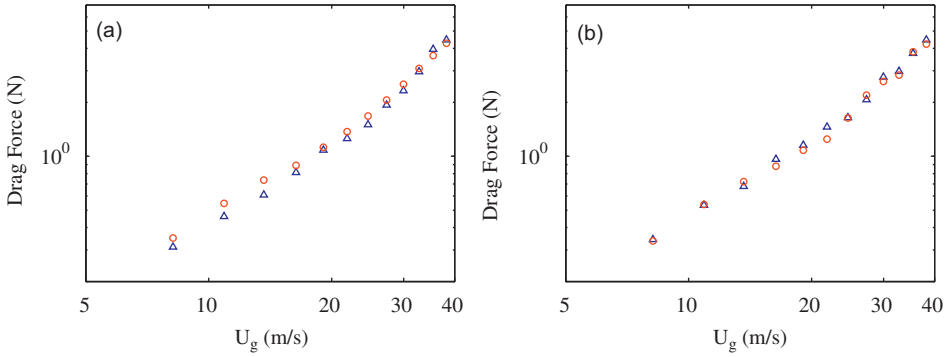

Fig. 22. $P/d = 1.58$; drag force: △, test 1; ○, test 2. (a) $y/d = 0\%$; (b) $y/d = 5\%$.

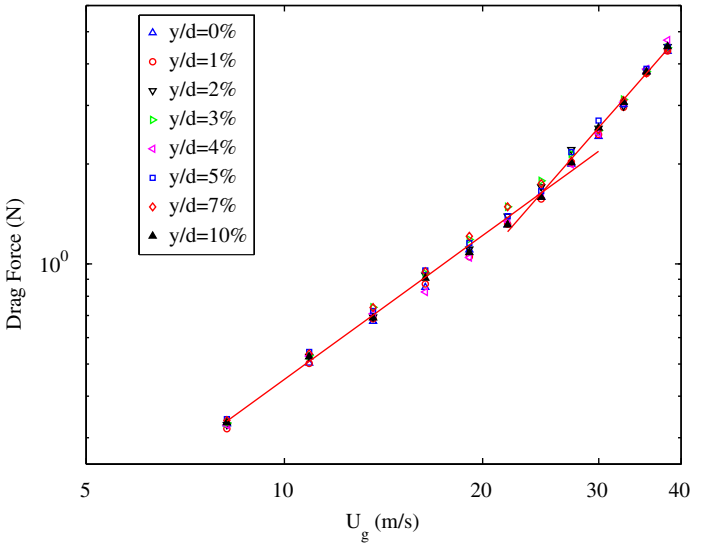

Fig. 23. $P/d = 1.58$; drag force at all tube displacements with fitted lines.

of 1.4 and 2.3 were obtained for the lower and higher Reynolds numbers, respectively. This change in behaviour suggests a transition from one flow regime to another and it occurs at $\mathrm{Re} \approx 6.6 \times 10^4$.

Using the same approach outlined for the pitch ratio of 1.32, a nondimensional relationship between drag coefficient and Reynolds number was obtained:

$$C_D = k\,\mathrm{Re}^n,$$

$$\mathrm{Re} < 6.6 \times 10^4 \begin{cases} k = 298, \\ n = -0.6, \end{cases}$$

$$\mathrm{Re} > 6.6 \times 10^4 \begin{cases} k = 0.0138, \\ n = 0.3. \end{cases} \tag{10}$$

The relationship between drag coefficient and Reynolds number is also shown in Fig. 24. The pitch ratio of 1.58 requires two sets of indices equations to represent the data above and below $\mathrm{Re} \approx 6.6 \times 10^4$ due to the change in the flow behaviour reported above. The effect of tube displacement for this pitch ratio was small as detailed above. Hence, the indices in Eq. (10) can be applied at all tube displacements examined in this study.

For $P/d = 1.97$ the effect of tube displacement was smaller again. In fact the drag force data at all tube displacements collapsed very well. The data was parameterised using two lines as shown in Fig. 25. The indices obtained where 1.4 and 2 for the lower and higher Reynolds numbers, respectively, with the transition in the flow regime occurring at a slightly higher Reynolds number ($\approx 6.8 \times 10^4$), than for $P/d = 1.58$. An analysis similar to that performed on the other pitch ratios was carried out. The relationship between drag coefficient and Reynolds number was similar to that observed for the pitch ratio of 1.58. However, the index, n and constant k for the lower and higher Reynolds number range were different and are shown below:

$$C_D = k\mathrm{Re}^n,$$

$$\mathrm{Re} < 6.8 \times 10^4 \begin{cases} k = 319, \\ n = -0.6, \end{cases}$$

$$\mathrm{Re} > 6.8 \times 10^4 \begin{cases} k = 0.396, \\ n = 0. \end{cases} \tag{11}$$

The relationship between drag coefficient and Reynolds number described by Eq. (11) is shown in Fig. 26. At the higher Reynolds number range it is observed that the index is equal to zero. This implies that the drag

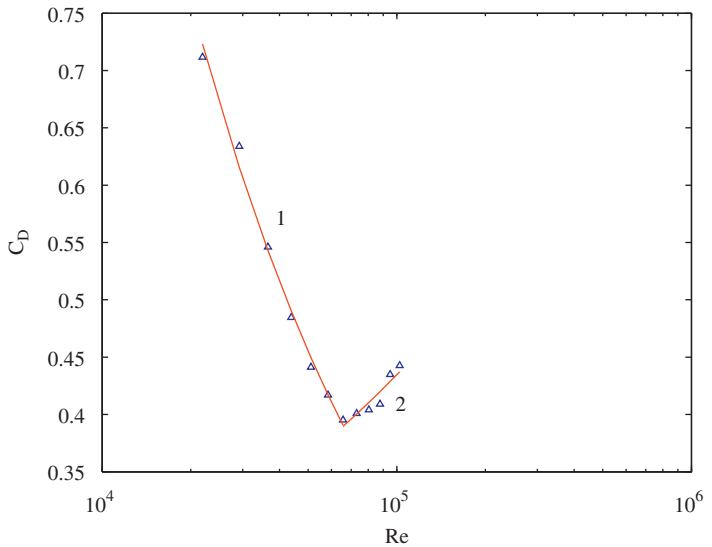

Fig. 24. $P/d = 1.58$; drag coefficient (averaged for all tube displacements) against Reynolds number.

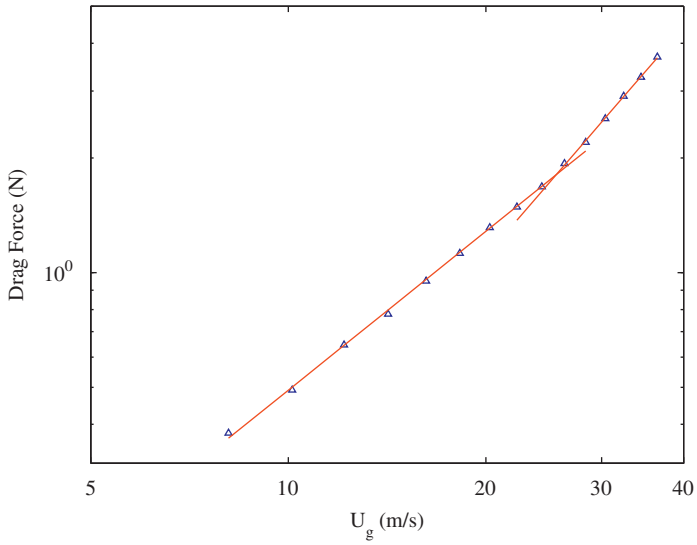

Fig. 25. $P/d = 1.97$; drag force (averaged for all tube displacements).

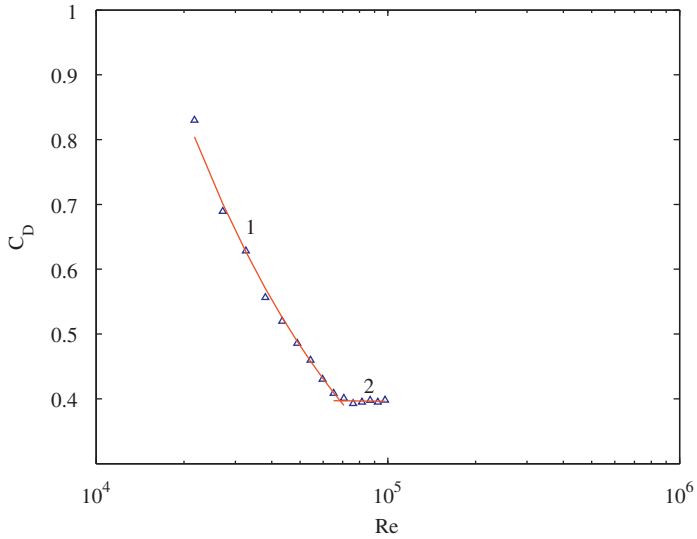

Fig. 26. $P/d = 1.97$; drag coefficient (averaged for all tube displacements) against Reynolds number.

coefficient becomes independent of Reynolds number and hence, in this instance the drag force scales proportionally to dynamic head.

For the pitch ratio of 1.32 the effect of tube displacement on pressure distribution was clearly observable, however, the effect on the drag force was small. In $P/d = 1.58$ the effect of tube displacement was smaller with the bulk changes in pressure occurring at $\pm 90^\circ$ and the regions fore and aft. However, the contribution to the drag force in these regions was small. For $P/d = 1.97$ the effect of tube displacement was reduced further. For all arrays it was found that displacing the cylinder changed the pressure distribution at the front of the cylinder where the contribution to the drag force was more significant. However, the changes in pressure were generally not converted into a net change in drag force. Hence, the contribution from the tube displacement to alter the drag force was deemed to be small as well. These findings suggest that the drag force was largely dependent on the bulk pressure drop across the array and was only weakly dependent on local flow characteristics. It was also apparent that the drag force does not scale proportionally with dynamic head with the exception of the sparsest array ($P/d = 1.97$) at the higher Reynolds numbers tested.

3.4.2. Lift force

The lift force is given the same form as the drag force with the drag coefficient term, C_D, being replaced with the lift coefficient term, $C_L = F_L(\frac{1}{2}\rho dl U_g^2)$. For $P/d = 1.32$ the lift force around a cylinder in an array appears to be very well behaved. When $y/d = 0\%$ the lift force fluctuated around zero. When the tube was displaced, a net lift force in the direction opposite to the tube displacement results. The magnitude of the force generally increased with tube displacement and flow velocity. This is more clearly observable from Fig. 27 which plots the lift coefficient against Reynolds number. C_L increases at the lower Reynolds number range tested. As the Reynolds number is increased further the rate of change reduces and at the higher Reynolds numbers C_L starts to reduce. This occurs at all tube displacements.

Although the lift force was well behaved, increasing in magnitude with increasing displacement and flow velocity, no simple parameterisation in terms of displacement and flow velocity was found. Normalising the lift force with respect to various different parameters did not collapse the data. This was because the lift force was far more susceptible to a change in displacement than the drag force. In fact, the lift force increases from ~0.5 to ~3 N, when the tube displacement increased from 1% to 10%. The upper value of the lift force approximately corresponds to ~40% of the

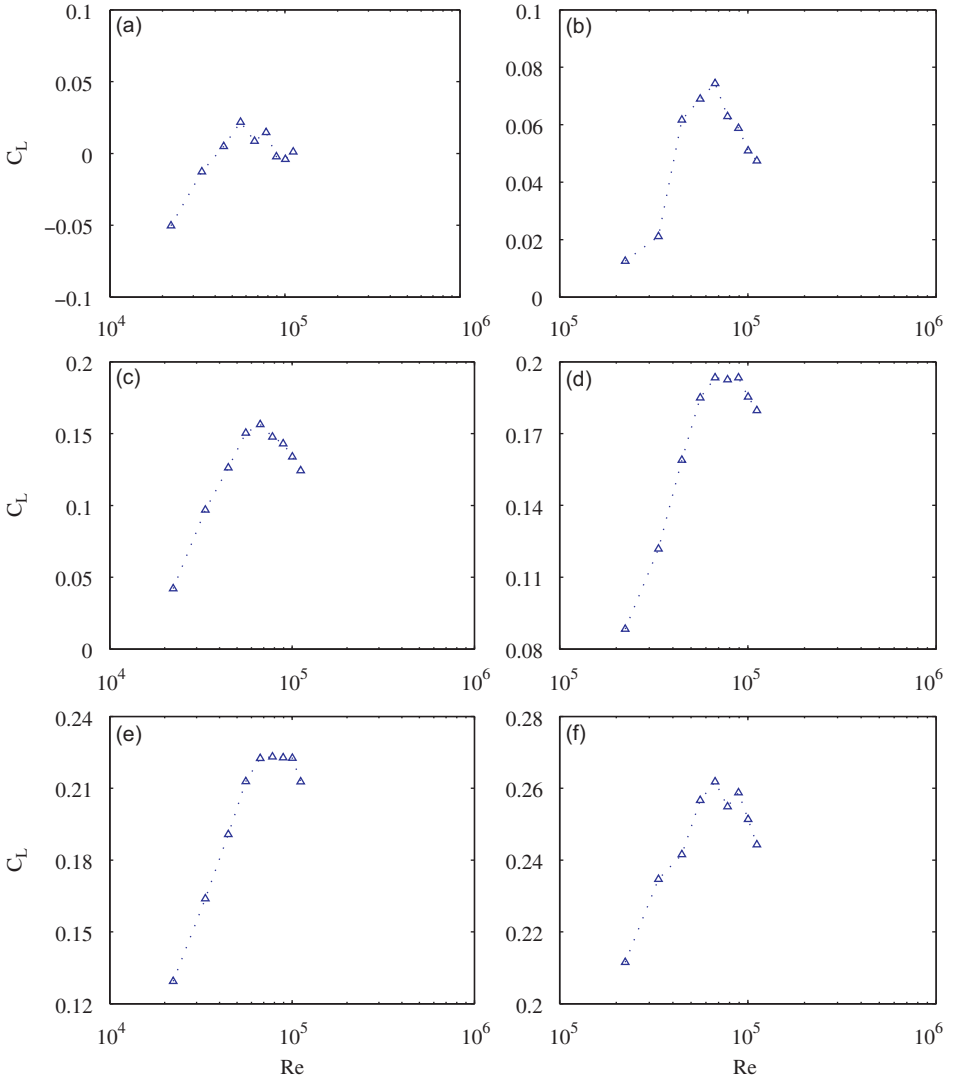

Fig. 27. $P/d = 1.32$; lift coefficient against Reynolds number at various tube displacements: (a) $y/d = 0\%$; (b) $y/d = 1\%$; (c) $y/d = 3\%$; (d) $y/d = 5\%$; (e) $y/d = 7\%$; (f) $y/d = 10\%$.

drag force for the same setup and conditions. Unlike the drag coefficient, the lift force was not as dependent on the bulk pressure drop across the array but was influenced by the local flow characteristics.

The lift force for the pitch ratio of 1.58 was more complex than the pitch ratio 1.32. This was as a result of the flow instability observed in the pitch ratio of 1.58. The lift force increased with tube displacement, however, on some occasions the force increase was more significant and/or the force was in the opposite direction. When the data is plotted in terms of the lift coefficient there is significant scatter for the aforementioned reasons. However, the magnitude of the lift coefficient generally increases with tube displacement as shown in Fig. 28. Again no simple parameterisation was found in terms of flow velocity.

The results presented for the pitch ratio of 1.97 showed asymmetry in the pressure distribution the form of which varied with flow velocity. This resulted in a peculiar effect, with the lift force fluctuating about zero at lower Reynolds numbers and a net force generated at higher Reynolds numbers. This was not attributed to a rotational offset and can only be explained by a flow-induced phenomenon. Examining the time-resolved pressure signal showed no flow instability. Flow visualisation was attempted to further understand the nature of the flow but proved to be unsuccessful. It was observed that different magnitudes of fluctuations were found on both sides of the cylinder suggesting differences in the wake of the leeward cylinder. However, further experiments are required to better understand the pitch ratio of 1.97.

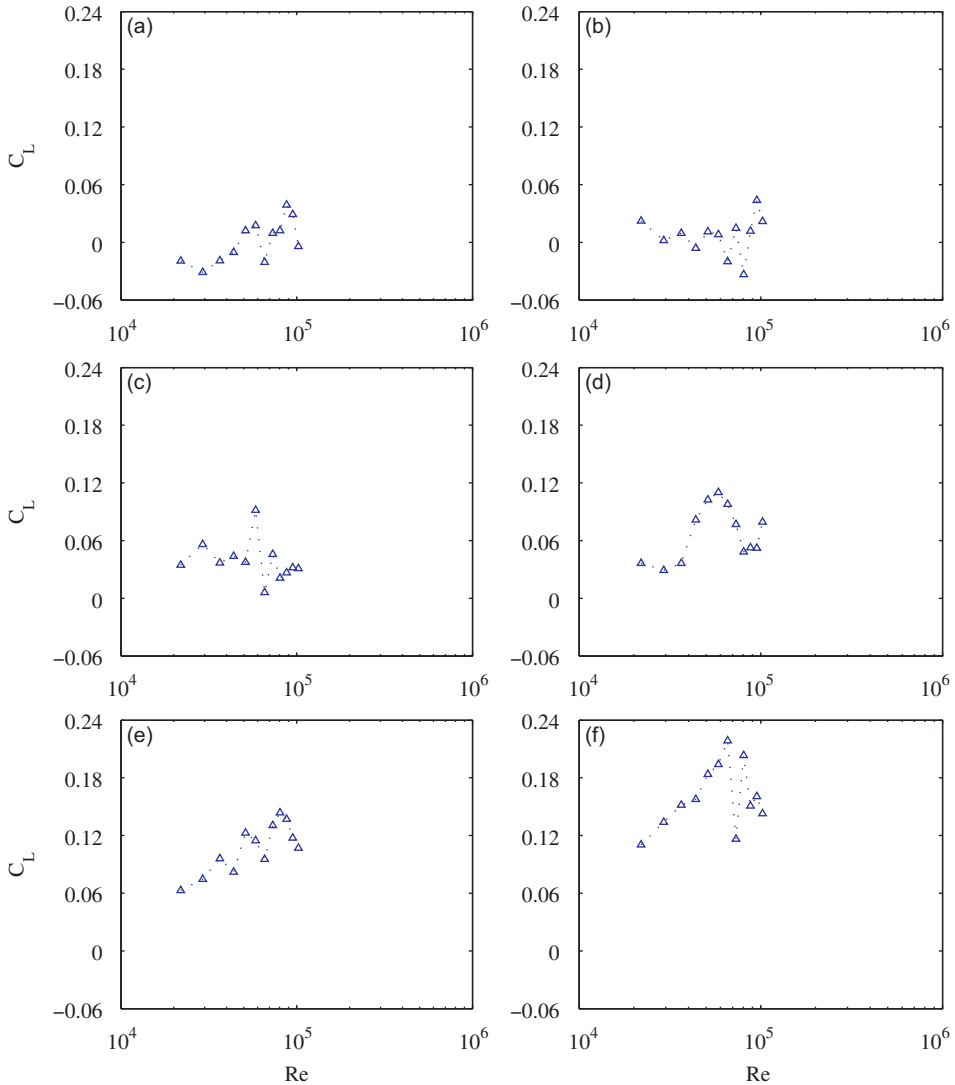

Fig. 28. $P/d = 1.58$; lift coefficient against Reynolds number at various tube displacements: (a) $y/d = 0\%$; (b) $y/d = 1\%$; (c) $y/d = 3\%$; (d) $y/d = 5\%$; (e) $y/d = 7\%$; (f) $y/d = 10\%$.

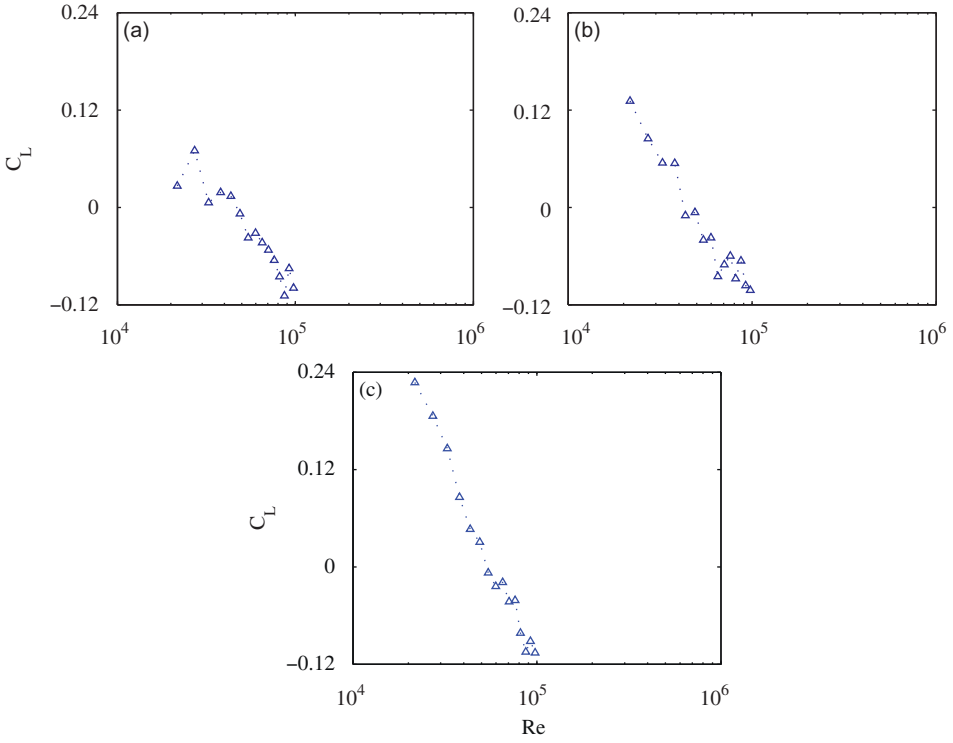

Fig. 29. $P/d = 1.97$; lift coefficient against Reynolds number at various tube displacements: (a) $y/d = 0\%$; (b) $y/d = 5\%$; (c) $y/d = 10\%$.

The peculiarity in the lift data for $P/d = 1.97$ results in the lift coefficient (Fig. 29) decreasing with Reynolds number. So much so at the higher Reynolds number range the lift coefficient becomes negative.

As reported above, no simple parameterisation between lift force and flow velocity was obtained. In this instance it is clear that the lift force is a function of flow velocity, tube displacement and array geometry (including both array configuration and pitch) and this must be taken into account when including the lift force in models.

4. Conclusions

Base-line surface pressure measurements for a tube in the third row of three normal triangular tube arrays have been performed. Pressure measurements were also made with various static displacements applied to the tube. This data provides a reference for the validation of simulations of fluidelastic instability in normal triangular tube arrays. The flow structure in the pitch ratio of 1.58 was unstable and bi-stable flow instability was observed even when geometric symmetry was broken.

The fluid forces did not scale with dynamic head as assumed by models in the literature. It was found that the fluid forces which are related to fluidelastic instability are dependent on Reynolds number and pitch ratio. A nondimensional relationship between drag coefficient and Reynolds number was found for all three arrays. For $P/d = 1.32$ the equation included tube displacement. This was not required for the other pitch ratios as the effect of tube displacement was small. However, the change in the flow regime observed for $P/d = 1.58$ and 1.97 resulted in different indices and constants for lower and higher Reynolds number ranges.

For $P/d = 1.32$ the lift force behaved well, increasing with flow velocity and tube displacement. For $P/d = 1.58$ this well-structured behaviour was interrupted by the flow instability. $P/d = 1.97$ showed a peculiar lift distribution requiring further investigation. For all array pitches tested, no simple parameterisation was found for the lift force as it was observed to be highly dependent on the flow velocity, array geometry and tube displacement.

Acknowledgement

This publication has emanated from research conducted with the financial support of Science Foundation Ireland.

References

Achenbach, E., 1969. Investigations on the flow through a staggered tube bundle at Reynolds numbers up to $Re = 10^7$. Wärme und Stoffübertragung Bd 2, 47–52.

Batham, J.P., 1973. Pressure distribution on in-line tube arrays in cross flow. In: International Symposium on Vibration Problems in Industry, Keswick, UK, Paper 411.

Connors, H.J., 1970. Fluidelastic vibration of tube arrays excited by cross flow. In: Reiff, D.D. (Ed.), Flow-Induced Vibration in Heat Exchangers. ASME, New York, pp. 42–56.

Lever, J.H., Weaver, D.S., 1986. On the stability of heat exchanger tube bundles. Parts 1 and 2. Journal of Sound and Vibration 107, 375–410.

Ljungkrona, L., Norberg, C., Sundén, B., 1991. Free-stream turbulence and tube spacing effects on surface pressure fluctuations for two tubes in an in-line arrangement. Journal of Fluids and Structures 5, 701–727.

Mahon, J., 2008. Interaction between acoustic resonance and fluidelastic instability in a normal triangular tube arrays. Ph.D. Thesis, Trinity College Dublin.

Price, S.J., Païdoussis, M.P., 1984a. An improved mathematical model for the stability of cylinder rows subject to cross-flow. Journal of Sound and Vibration 97, 615–640.

Price, S.J., Païdoussis, M.P., 1984b. The aerodynamic forces acting on groups of two and three circular cylinders when subject to a cross flow. Journal of Wind Engineering and Industrial Aerodynamics 17, 329–347.

Price, S.J., 1995. A review of theoretical models for fluidelastic instability of cylinder arrays in cross-flow. Journal of Fluids and Structures 9, 463–518.

Ting, D.S.K., Wang, S.J., Price, S.J., 1998. Paidoussis, An experimental study on the fluidelastic forces for two staggered circular cylinders in cross-flow. Journal of Fluids and Structures 12, 259–294.

Zdravkovich, M.M., Namork, J.E., 1980. Excitation, amplification and suppression of flow-induced vibration in heat exchangers. In: Practical Experiences with Flow Induced Vibrations, Paper A5, pp. 107–117.

Zdravkovich, M.M., Stonebanks, K.L., 1990. Intrinsically nonuniform and metastable flow in and behind tube arrays. Journal of Fluids and Structures 4, 305–319.

Zdravkovich, M.M., 1993. On suppressing metastable interstitial flow behind a tube array. Journal of Fluids and Structures 7, 245–252.

Žukauskas, A.A., Ulinskas, R.V., Bubelis, E.S., 1983. Heat transfer in separated flows at Re between 1 and 2×10^6 and Pr between 0.7 and 10,000 (separation of vortices from tubes). Heat Transfer—Soviet Research 15, 73–80.

Žukauskas, A., 1989. Cylinders in crossflow, High-Performance Single-Phase Heat Exchangers. Hemisphere Publishing Corporation, pp. 187–206 (Chapter 10).